JGR Solid Earth

RESEARCH ARTICLE
10.1029/2018JB016485

Special Section:
Merging Geophysical, Petrochronologic and Modeling Perspectives to Understand Large Silicic Magma Systems

Magma Reservoir Below Laguna del Maule Volcanic Field, Chile, Imaged With Surface-Wave Tomography

Crystal E. Wespestad[1], Clifford H. Thurber[1], Nathan L. Andersen[2], Brad S. Singer[1], Carlos Cardona[3], Xiangfang Zeng[4], Ninfa L. Bennington[1], Katie Keranen[5], Dana E. Peterson[5], Darcy Cordell[6], Martyn Unsworth[6], Craig Miller[7], and Glyn Williams-Jones[8]

[1]Department of Geoscience, University of Wisconsin-Madison, Madison, WI, USA, [2]Department of Earth Science, University of Oregon, Eugene, OR, USA, [3]Observatorio Volcanológico de los Andes del Sur, Servicio Nacional de Geología y Minería, Temuco, Chile, [4]State Key Laboratory of Geodesy and Earth's Dynamics, Institute of Geodesy and Geophysics Chinese Academy of Sciences, Wuhan, China, [5]Department of Earth and Atmospheric Sciences, Cornell University, Ithaca, NY, USA, [6]Department of Physics, University of Alberta, Edmonton, Alberta, Canada, [7]GNS Science, Taupo, New Zealand, [8]Centre for Natural Hazards Research, Department of Earth Sciences, Simon Fraser University, Burnaby, British Columbia, Canada

Abstract The Laguna del Maule (LdM) volcanic field comprises the greatest concentration of postglacial rhyolite in the Andes and includes the products of ~40 km^3 of explosive and effusive eruptions. Recent observations at LdM by interferometric synthetic aperture radar and global navigation satellite system geodesy have revealed inflation at rates exceeding 20 cm/year since 2007, capturing an ongoing period of growth of a potentially large upper crustal magma reservoir. Moreover, magnetotelluric and gravity studies indicate the presence of fluids and/or partial melt in the upper crust near the center of inflation. Petrologic observations imply repeated, rapid extraction of rhyolitic melt from crystal mush stored at depths of 4–6 km during at least the past 26 ka. We utilize multiple types of surface-wave observations to constrain the location and geometry of low-velocity domains beneath LdM. We present a three-dimensional shear-wave velocity model that delineates a ~450-km^3 shallow magma reservoir ~2 to 8 km below surface with an average melt fraction of ~5%. Interpretation of the seismic tomography in light of existing gravity, magnetotelluric, and geodetic observations supports this model and reveals variations in melt content and a deeper magma system feeding the shallow reservoir in greater detail than any of the geophysical methods alone. Geophysical imaging of the LdM magma system today is consistent with the petrologic inferences of the reservoir structure and growth during the past 20–60 kyr. Taken together with the ongoing unrest, a future rhyolite eruption of at least the scale of those common during the Holocene is a reasonable possibility.

Key Points:
- Results from a major deployment of seismic instruments at Laguna del Maule volcanic center are presented
- We use a novel application of multiple types of surface-wave dispersion data to infer 3D shear velocity structure
- We present a unified interpretation of results from seismology, geodesy, gravity, magnetotellurics, and petrochronology

Supporting Information:
- Supporting Information S1

Correspondence to:
C. H. Thurber,
cthurber@wisc.edu

Citation:
Wespestad, C. E., Thurber, C. H., Andersen, N. L., Singer, B. S., Cardona, C., Zeng, X., et al. (2019). Magma reservoir below Laguna del Maule volcanic field, Chile, imaged with surface-wave tomography. *Journal of Geophysical Research: Solid Earth*, *124*. https://doi.org/10.1029/2018JB016485

Received 30 JUL 2018
Accepted 19 FEB 2019
Accepted article online 21 FEB 2019

1. Introduction

Explosive silicic eruptions pose a substantial hazard to infrastructure and population centers (e.g., Castro & Dingwell, 2009; Self & Blake, 2008; Sparks et al., 2005). However, the scarcity of rhyolitic eruptions in the historical record limits understanding of their precursors and hampers efforts to anticipate their occurrence. Large silicic magma reservoirs, which are capable of producing both repeated modest-volume and large caldera-forming eruptions, are generally thought to comprise a crystal mush—a crystalline framework containing greater than ~40–50% crystals—from which less crystalline and thus eruptible magma batches may be extracted (Bachmann & Bergantz, 2004; Hildreth, 2004). A growing body of evidence indicates that shallow, eruptible (generally requiring >60% melt) magma bodies are ephemeral and that extensive crystal-rich reservoirs from which they are assembled may be destabilized rapidly when intercepted by ascending melt (e.g., Andersen, Jicha, et al., 2017; Andersen et al., 2018; Cooper & Kent, 2014; Druitt et al., 2012; Parks et al., 2012; Rubin et al., 2017; Singer et al., 2016; Szymanowski et al., 2017). Moreover, these eruptible magma chambers and the upper reaches of their surrounding crystal-rich reservoirs reflect transcrustal magma systems that extend vertically into the lower crust (Cashman et al., 2017). Yet the architecture of such transcrustal systems (Marsh, 2015), the mechanisms and rates of melt transport through their mostly cool crystalline mush columns (Jackson et al., 2018), and the thermochemical conditions required to generate and store significant volumes of eruptible magma in shallow chambers that form within them (Barboni et al., 2016; Cooper & Kent, 2014) all remain elusive.

Geophysical methods including interferometric synthetic aperture radar (InSAR) and global navigation satellite system (GNSS) geodesy, gravity, magnetotellurics (MT), and seismology offer means to constrain the dimensions and architecture of magma reservoirs and establish bounds for the conditions of magma storage (e.g., Hill et al., 2009; Lees, 2007; Lowenstern et al., 2006; Masterlark et al., 2010; Miller & Williams-Jones, 2016; Parks et al., 2012). Moreover, the capability to make several types of geophysical measurements of magmatic systems that are restless and growing in size as exhibited by surface inflation, and for which petrochronologic data are available, offers novel opportunities to better understand the dynamics of these potentially hazardous systems (Jay et al., 2014; Kukarina et al., 2017; Pritchard & Gregg, 2016; Singer et al., 2014). Although the detection of accumulated crystal-poor melt within a region of ongoing crustal deformation would represent a substantial volcanic hazard, to date, geophysical methods have not been able to clearly and consistently identify melt-rich magma reservoirs in the upper crust associated with large silicic systems (Comeau et al., 2016; Huang et al., 2015; Jaxybulatov et al., 2014; Ward et al., 2014) and thus have not contributed to this debate in a conclusive manner. In part, this is because various geophysical techniques are sensitive to different physical parameters and models derived from each method are inherently nonunique, such that they may produce apparently conflicting views of the same magma system (Pritchard & Gregg, 2016).

Here we present a three-dimensional (3D) shear-wave velocity (V_S) model for the restless, rhyolitic Laguna del Maule (LdM) volcanic field in the southern Andes (Hildreth et al., 2010; Singer et al., 2014). The rapid growth of the shallow magma reservoir, frequent eruption of rhyolite during the late Pleistocene to Holocene, plus long-term and modern unrest accompanied by episodic surface inflation collectively suggest LdM may currently be building toward an explosive, potentially large, eruption (Hildreth et al., 2010; Singer et al., 2014. Singer et al., 2018).The V_S model reveals an upper crustal magma reservoir of several hundred cubic kilometers dominated by crystal-rich conditions located near the center of ongoing surface deformation.

Other published observations that are integrated into our interpretations are the following: (1) geodetic surveys using InSAR and GNSS data (Feigl et al., 2014; Le Mével et al., 2015, 2016), (2) gravity measurements and the 3D density distribution (Miller et al., 2017), (3) an MT survey and 3D electrical resistivity structure (Cordell et al., 2018), (4) petrochronologic findings from several rhyolitic eruptive products (Andersen, Singer, et al., 2017; Andersen et al., 2018), and (5) geomorphic evidence that the LdM magma reservoir has grown rapidly during the Holocene (Singer et al., 2018). The combined observations provide more detailed constraints on the size, geometry, melt content, and dynamics of the modern LdM magma system. The integration of these observations reveals that the modern, shallow LdM magma reservoir (1) is laterally offset from its deeper, transcrustal roots; (2) persists dominantly at near-solidus conditions but contains smaller-volume (<20 km^3) melt-rich lenses; and (3) is consistent with the continuation of at least 40 kyr of magmatism at LdM that has catalyzed the frequent eruption of rhyolite over the last 20 kyr.

2. Geologic Setting and Existing Geophysical Data

LdM sits atop the southern Andean range crest where a flare-up of dominantly silicic volcanism occurred during the past 20,000 years (Figure 1a; Andersen, Singer, et al., 2017; Hildreth et al., 2010). The rhyolite lava flow of Las Nieblas (Figure 1a) is among the most recent eruptions within the LdM basin, most likely during the last 2,000 years (Andersen, Singer, et al., 2017; Fierstein, 2018; Hildreth et al., 2010). The silicic eruptions include effusive and explosive events and are volumetrically dominated by crystal-poor rhyolite, with less voluminous rhyodacite and andesite eruptions concentrated in the northwestern to western LdM basin outside the periphery of rhyolitic vents (Figure 1a). Rhyolite at LdM is generated by differentiation of mafic to intermediate precursors in the upper crust (4- to 6-km depth) by fractional crystallization with subordinate assimilation of partially solidified magma bodies emplaced during the late Pleistocene as well as plutonic and volcanic wall rocks comprising a young upper crust (Andersen, Singer, et al., 2017). This shallow magmatism is the uppermost expression of a long-lived transcrustal magma system (Cashman et al., 2017) reflecting hundreds of thousands of years of Quaternary magma flux that extends upward from the deep crust and comprises polybaric domains of magma storage and crustal assimilation (Andersen, Singer, et al., 2017; Hildreth & Moorbath, 1988). Complex mineral zoning and ubiquitous centimeter-scale chilled mafic inclusions within the rhyodacite lavas record the ascent of mafic to intermediate magma

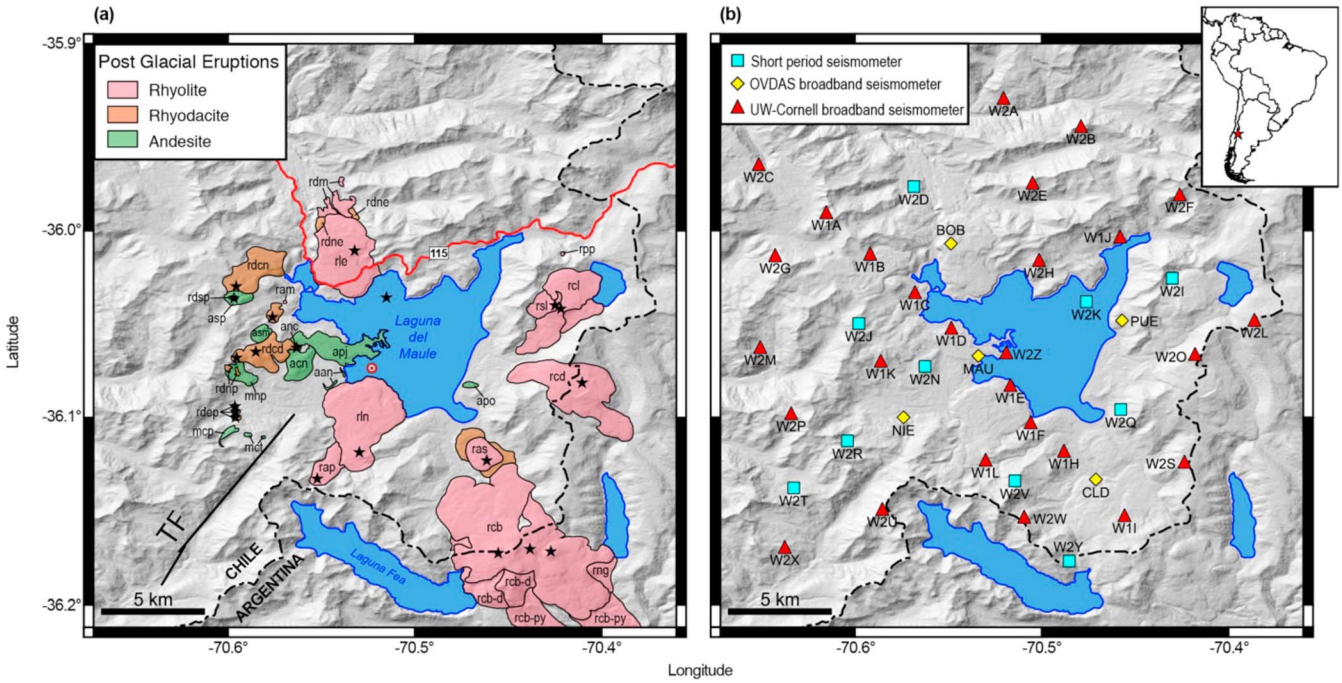

Figure 1. Shaded relief maps of central Laguna del Maule (LdM) volcanic field. (a) Simplified postglacial geology of LdM volcanic field, modified from Hildreth et al. (2010) and Andersen, Singer, et al. (2017). The stars are volcanic vents, and the bull's-eye is the approximate center of ongoing uplift at >20 cm/year (Feigl et al., 2014). TF = Troncoso fault (black line). Red line = road. (b) The seismic stations at LdM volcanic field used in this study.

throughout postglacial time. However, such magmas rarely erupted within the locus of rhyolite volcanism (Figure 1a); the rhyolites are mostly free of mafic inclusions and host a dominantly homogeneous plagioclase population indicative of unperturbed in situ crystallization. Accordingly, it is hypothesized that a substantial magma reservoir resides beneath LdM that intercepts the ascent of less evolved magmas and serves as the source for rhyolite magma bodies that have repeatedly accumulated and erupted from its upper reaches (Andersen et al., 2018; Andersen, Singer, et al., 2017; Hildreth et al., 2010; Singer et al., 2018).

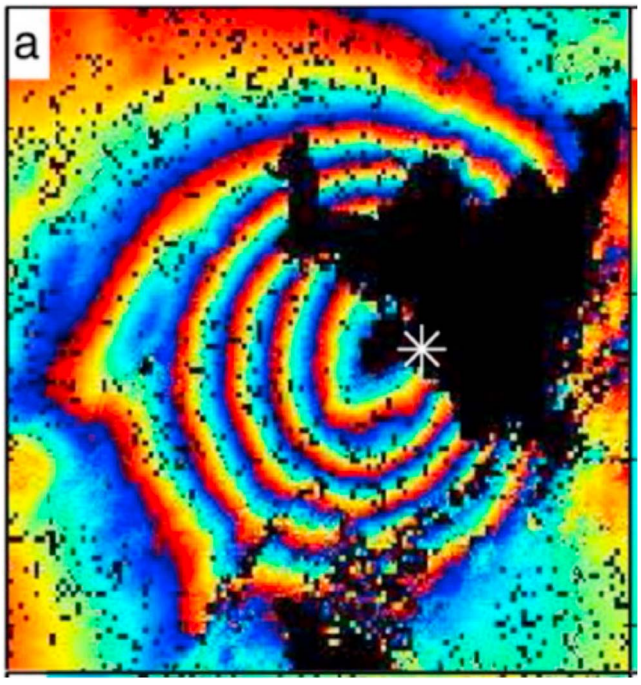

Figure 2. Deformation pattern from 3 years of interferometric synthetic aperture radar observations (Feigl et al., 2014).

Recent observations at LdM by InSAR and GNSS satellite geodesy have revealed inflation at rates exceeding 20 cm/year since 2007 (Feigl et al., 2014; Fournier et al., 2010; Le Mével et al., 2015, 2016) (Figure 2). This episode of inflation has been explained by a model of a transient supply of magma into a reservoir at 4.5-km depth (below surface) and requires recharge at a rate of 0.03–0.04 km^3/year (Le Mével et al., 2016). Such a flux is sufficient to destabilize a cool silicic magma reservoir (Druitt et al., 2012; Parks et al., 2012). This current inflation and unrest may be the most recent of many episodes that have warped the surface of the LdM basin more than 60 m as the shallow magma reservoir grew during the Holocene (Singer et al., 2018). Petrologic constraints suggest that the accumulation of fluids derived from intruding magma may be an important mechanism by which rhyolite eruptions have been triggered at LdM (Andersen et al., 2018). The occurrence of earthquake swarms and long-period earthquakes (Cardona et al., 2018) as well as diffuse CO_2 soil degassing (Miller et al., 2017) is also consistent with the presence of magmatic fluids. Thus, the ongoing unrest may capture the growth and possibly the destabilization of a potentially large, rhyolitic upper crustal magma reservoir that could culminate in eruption (Singer et al., 2014).

A negative Bouguer gravity anomaly is spatially coincident with the current uplift (Miller, Williams-Jones, et al., 2017). Inversion for the 3D density distribution supported by several hundred gravity observations made around the lake yields a model (supporting information Figure S1a) wherein a 30-km^3 low-density body at 2- to 4-km depth, containing a high melt percentage and exsolved fluids, is embedded within a 115-km^3 domain from ~1.5- to 6-km depth. The 115-km^3 body is inferred to be crystal rich (<30% melt) based on the predicted density of cool intermediate to silicic LdM magma (Miller, Williams-Jones, et al., 2017).

Recent MT measurements (Cordell et al., 2018) reveal low-resistivity bodies (C1 and C2) directly beneath the current center of inflation that are small and close to the surface (supporting information Figures S1b and S1c) but can be explained without the presence of partial melt. The C2 conductor is coincident with the source of positive gravity changes observed by Miller, LeMével, et al. (2017), which are interpreted as hydrothermal fluids migrating into the Troncoso fault (Figure 1a). The largest, lowest resistivity bodies (C3 and C4) that are more consistent with the presence of substantial melt are deeper (>6 km) and centered north of the lake (Cordell et al., 2018), away from most of the active Holocene vents and the focus of the ongoing unrest.

3. Surface-Wave Tomography

The locations of the seismic stations used in our analysis of the modern LdM magma system are shown in Figure 1b. Surface-wave dispersion data are obtained using three different processing methods. We utilize continuous data from a local array of 43 seismic instruments spread over an area about ~30 by 30 km with a typical station spacing of 3 to 5 km (Figure 1b). There is a large gap in the center of the array due to the presence of the lake, with the exception of an instrument on a peninsula in the west and on an island in the northeast corner of the lake.

We used the novel strategy of assembling frequency-dependent surface-wave traveltime data from three different methods in order to maximize the amount of good-quality data for a larger range of frequencies. The two main criteria for assessing data quality were signal-to-noise ratio and stability of the dispersion curve with frequency. Surface-wave data were obtained via (1) ambient noise cross-correlation between station pairs in the local array (Figure 1b), (2) regional earthquake coda correlation between local station pairs (Figure 3a), and (3) differential dispersion from ambient noise cross-correlation of data from remote stations with stations in the local array (Figure 3b).

Method 1 has emerged as a standard technique for imaging V_S structure with continuously recorded data from seismic arrays (Campillo et al., 2011). It works best with a reasonably uniform directional distribution of noise sources. Method 2 can be effective when the noise source distribution is nonideal, because coda waves arise from random scattering effects and thus typically propagate in all directions (Campillo & Paul, 2003). These two methods yield group velocity measurements extracted from the cross-correlation functions between local stations. The symmetrical component (the average of the negative time and positive time parts, as in Bensen et al., 2007) is filtered with a series of Gaussian narrow band-pass filters, and then the arrival time is picked on the envelope of the filtered trace at the arrival time of maximum energy. This process is known as multiple-filter analysis or frequency-time analysis (Feng & Teng, 1983). Some examples are shown in supporting information Figure S2.

Method 3 is a hybrid of the standard two-station method for surface-wave dispersion measurement from earthquakes with the ambient noise approach, comparable with that of Yang (2014). A remote station serves as a "virtual earthquake," and the difference in the dispersion measured with frequency-time analysis at two stations within the local array yields an estimate of the dispersion between the two local stations. We restrict the difference in azimuth to the remote station to be less than 10° and correct for the off-great-circle effect on distance (see supporting information Figure S3). The error introduced by this approximation is only a few percent at most (Yao et al., 2006). For quality control, we only include data from station pairs that have cross-correlation functions with a correlation coefficient of 0.7 or higher. An example of the move-out of the Rayleigh wave across the array that is observable in the cross-correlation functions is shown in Figure 3c. This method measures phase velocity and can reach lower frequencies (longer wavelengths) due to the longer propagation path between the remote stations and the local array. This allows for the resolution of structure to greater depths than does either of the other two methods.

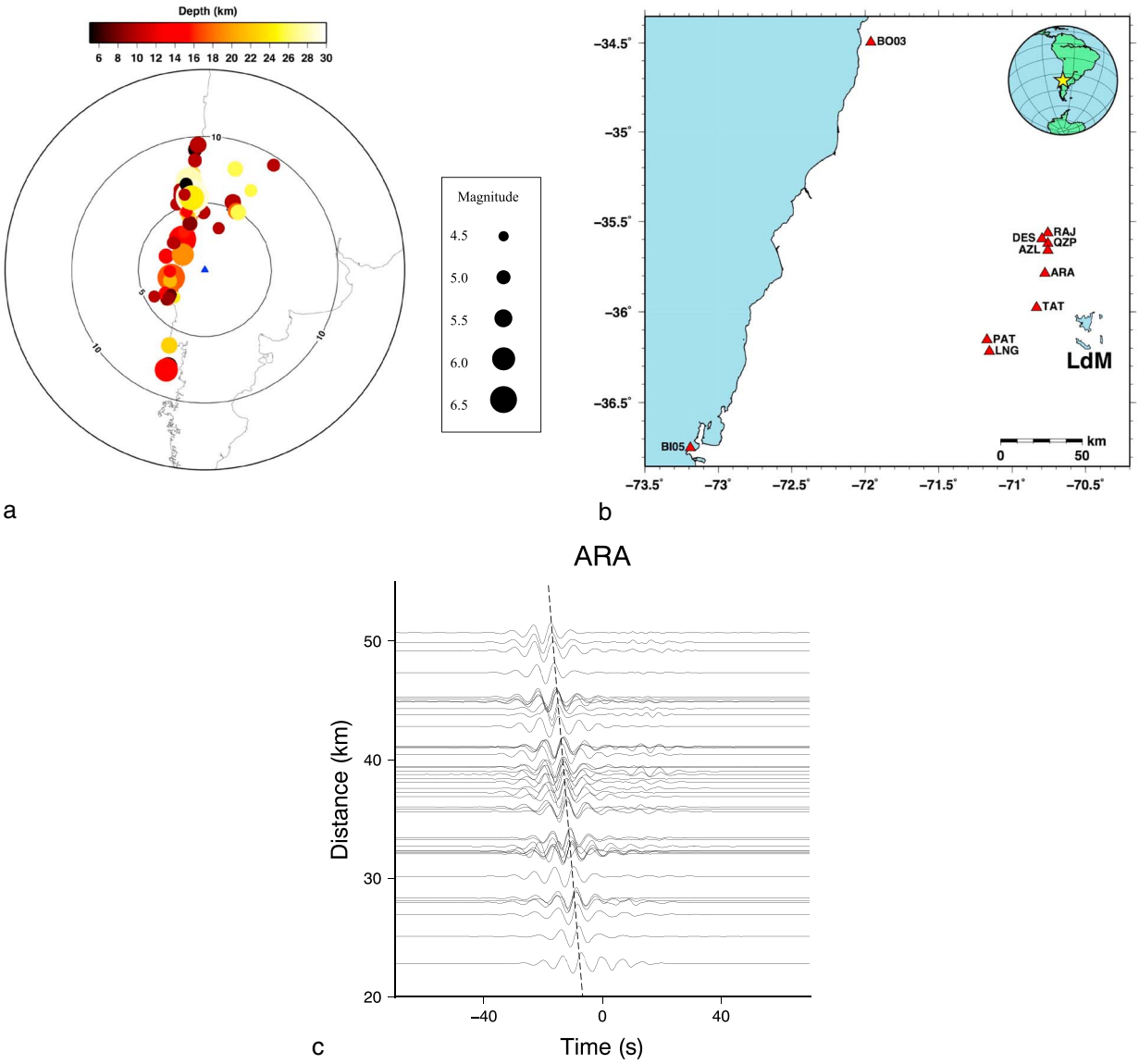

Figure 3. (a) Map of earthquakes (colored circles) used for the coda correlation analysis. Laguna del Maule (LdM) is the blue triangle. Circles are at 5° epicentral distance intervals. Circle size corresponds to moment magnitude of the earthquakes, ranging from 4.5 to 6.3. (b) Map of stations used for the remote station-noise correlation method. (c) Example of move-out of cross-correlation functions as a function of distance of the array stations from remote station ARA. The dashed line indicates a velocity of 3 km/s.

Each method produces usable results for a certain frequency band: method 1, local-local noise, for 0.23–0.39 Hz; method 2, regional earthquake coda, for 0.23–0.31 Hz; and method 3, remote-local noise, for 0.09–0.21 Hz. By capitalizing on the use of both ambient noise and coda correlation data, we nearly doubled the number of usable station-to-station paths for our tomographic inversions compared with using method 1 alone.

After the group or phase traveltimes between station pairs are obtained for a range of frequencies from the correlation results, a standard two-step approach is used to obtain a 3D V_S model from the dispersion results: (1) inversion for two-dimensional (2D) group and phase velocity maps followed by (2) cell-by-cell inversions for V_S versus depth below surface (Bensen et al., 2007; Masterlark et al., 2010), which in this case is at an average of approximately 2,500 m above the WGS84 ellipsoid.

The group and/or phase velocity inversions for the 2D maps at different frequencies were carried out using the simul2000 algorithm (Thurber & Eberhart-Phillps, 1999). Although developed originally for 3D local

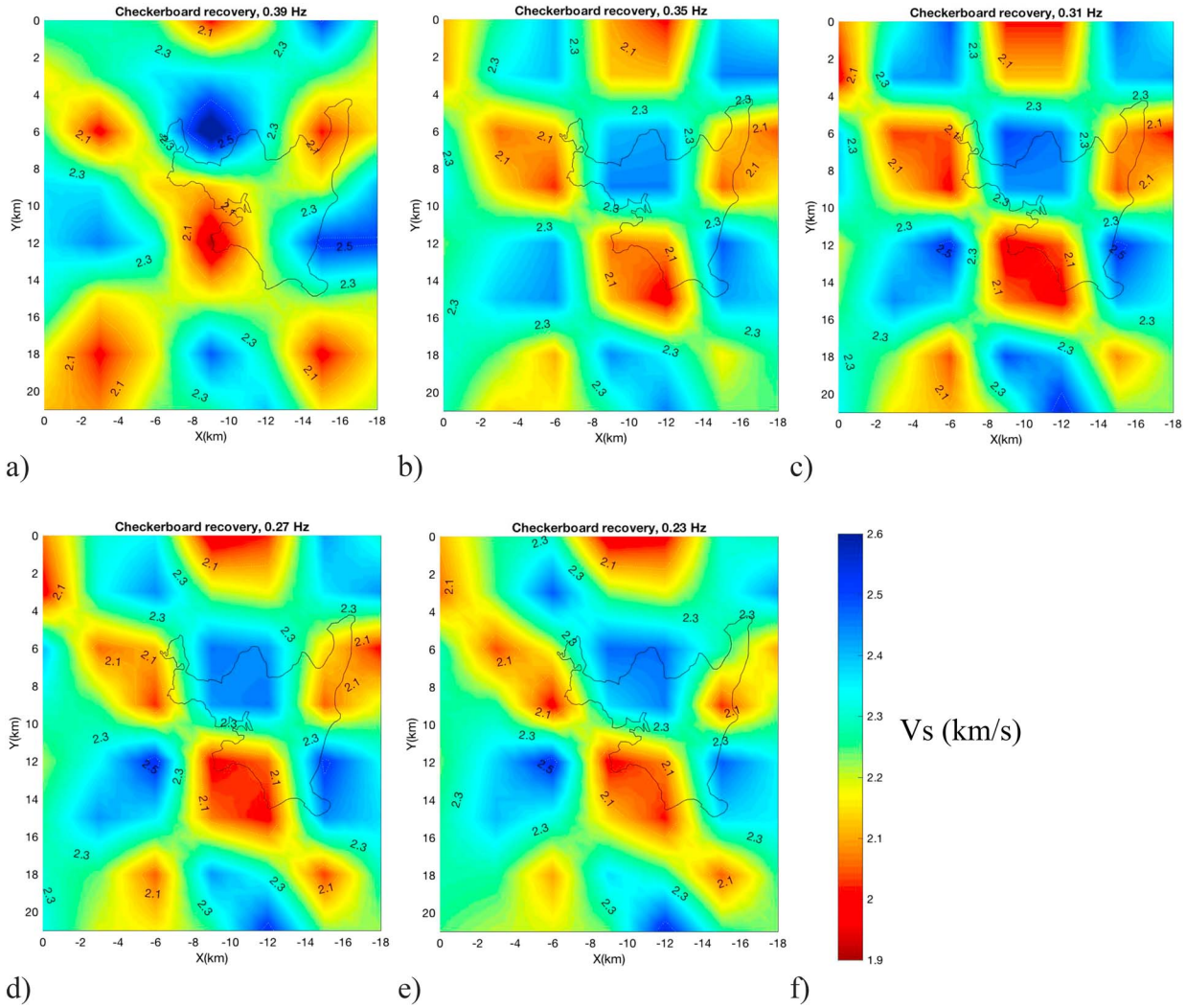

Figure 4. Checkerboard test results for representative frequencies. (a) 0.39 Hz. (b) 0.35 Hz. (c) 0.31 Hz. (d) 0.27 Hz. (e) 0.23 Hz. (f) Color scale for (a)–(e).

earthquake tomography, it readily handles data for fixed source locations, in this case, one station of the pair, the virtual source. It can also solve for 2D models, in this case velocity as a function of the two horizontal coordinates. The simul2000 code employs pseudo-bending ray tracing in 2D (Um & Thurber, 1987) and solves the inversion using iterative damped least squares with a full matrix inversion. The latter allows for the direct computation of the model resolution and model covariance matrices (Aster et al., 2012). A detailed trade-off analysis was carried out to select an appropriate parameter value. Damping values at factors of 2 between 2.5 and 160 were tested, with a value of 20 providing a good data fit, acceptable model resolution, and good recovery of checkerboard anomalies. The checkerboard tests are shown in Figure 4, and maps showing the diagonal element of the model resolution matrix for each node are provided (supporting information Figure S5) to complement the checkerboard tests. Variance reduction from the inversions is typically about 50%, with the final variance averaging about 0.4 s^2. An area of low velocity along the southwest side of the lake is evident in the resulting group and phase velocity maps (Figure 5).

We next use the frequency-dependent Rayleigh wave group and phase velocities at each node of the velocity maps to invert for local one-dimensional (1D) V_S models. Example 1D inversions are shown in supporting information Figure S4. The 1D models are then combined to produce the 3D V_S model. A map (at 4-km depth), cross sections, and perspective view of our 3D V_S model down to 11-km depth (relative to the average surface elevation) are shown in Figure 6. The principal anomaly is a zone of low V_S along the western

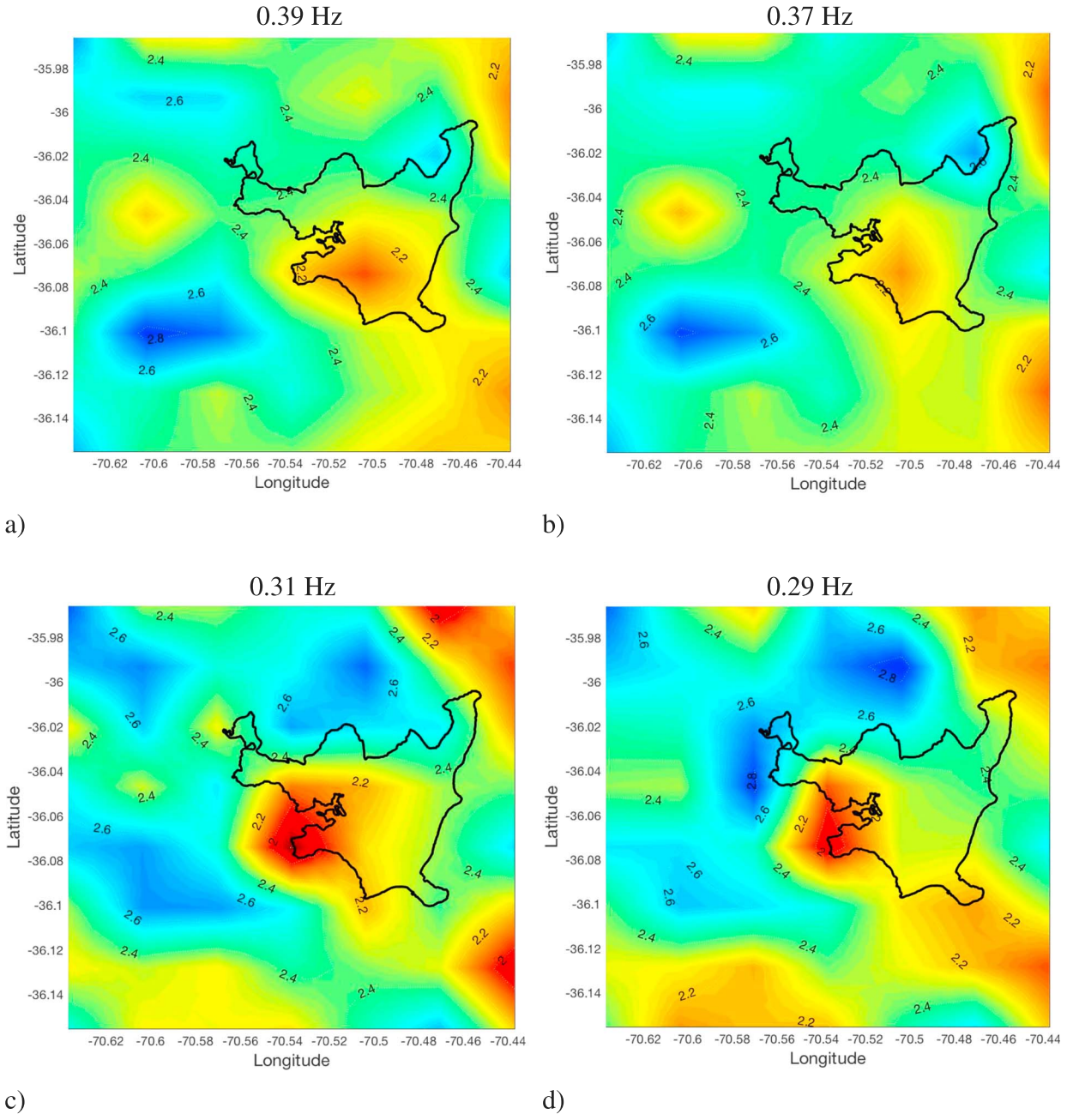

Figure 5. Representative (a–f) group and (g, h) phase velocity maps from our three-method analysis. Velocity values in km/s. (i) Color legend for (a)–(h).

perimeter of the lake, which is elongated in the northeast-southwest direction, dips steeply to the west, and has a roughly ellipsoidal shape.

4. Discussion

4.1. Estimation of Melt Fraction and Melt Volume

There is no consensus on the best method for inferring the size of a magma reservoir or its melt percentage from a low-velocity body in a V_S model (e.g., Lees, 2007; Magee et al., 2018) or from the other geophysical techniques discussed here. We use the depth range of the zone of reduced velocity at each latitude-

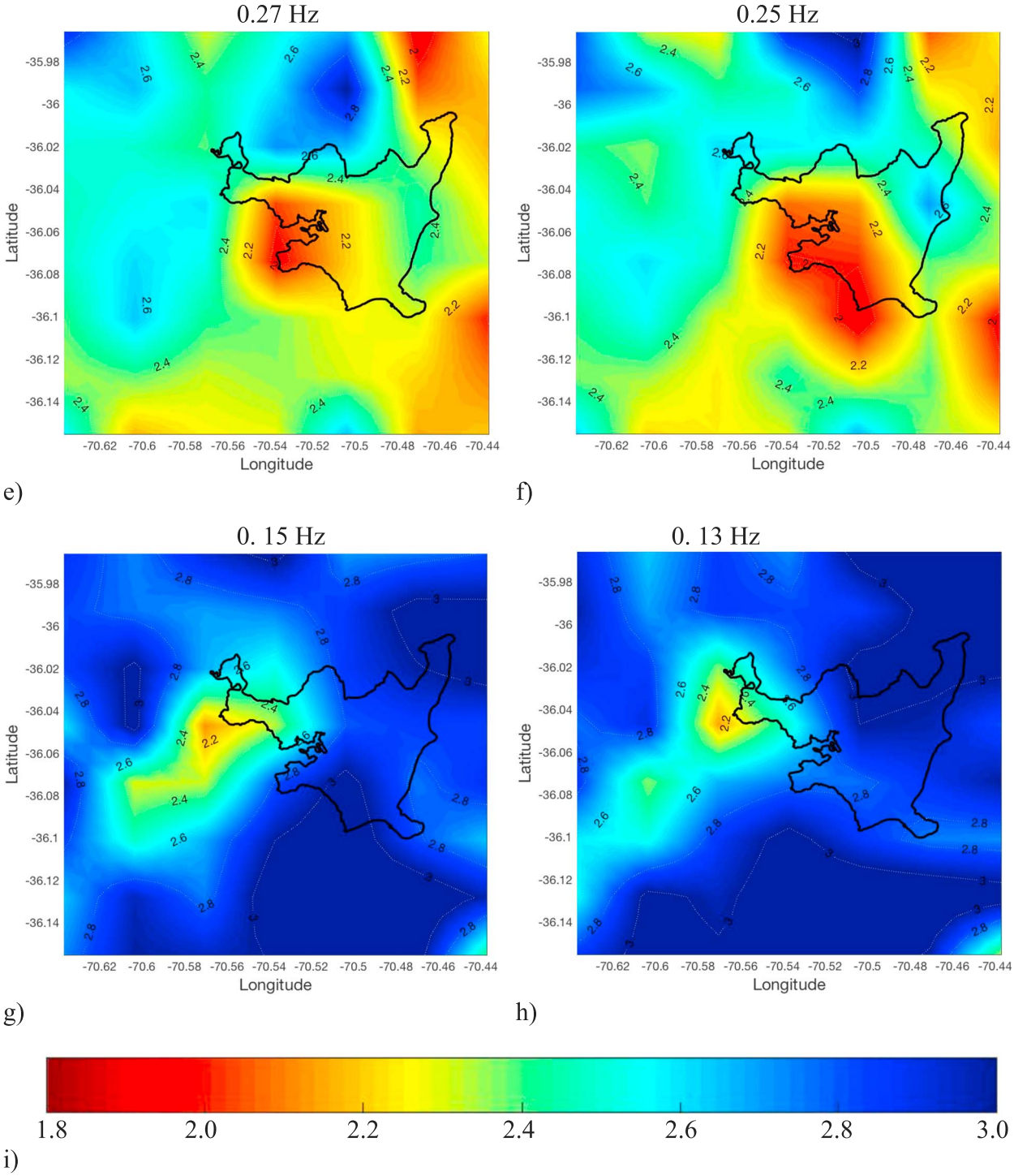

Figure 5. (continued)

longitude node point to represent the low-velocity body. We define the top by a change in the vertical velocity gradient from increasing with depth to decreasing with depth and the bottom by reaching the same velocity as at the top or reaching the depth where resolution is inadequate (supporting information Figure S7). This yields a volume estimate of ~450 km^3. Compared with average velocities of the surrounding material, this body has an average of a 12% (0.3–0.4 km/s) reduction in V_S and a maximum reduction of 28% (0.8 km/s) near its center.

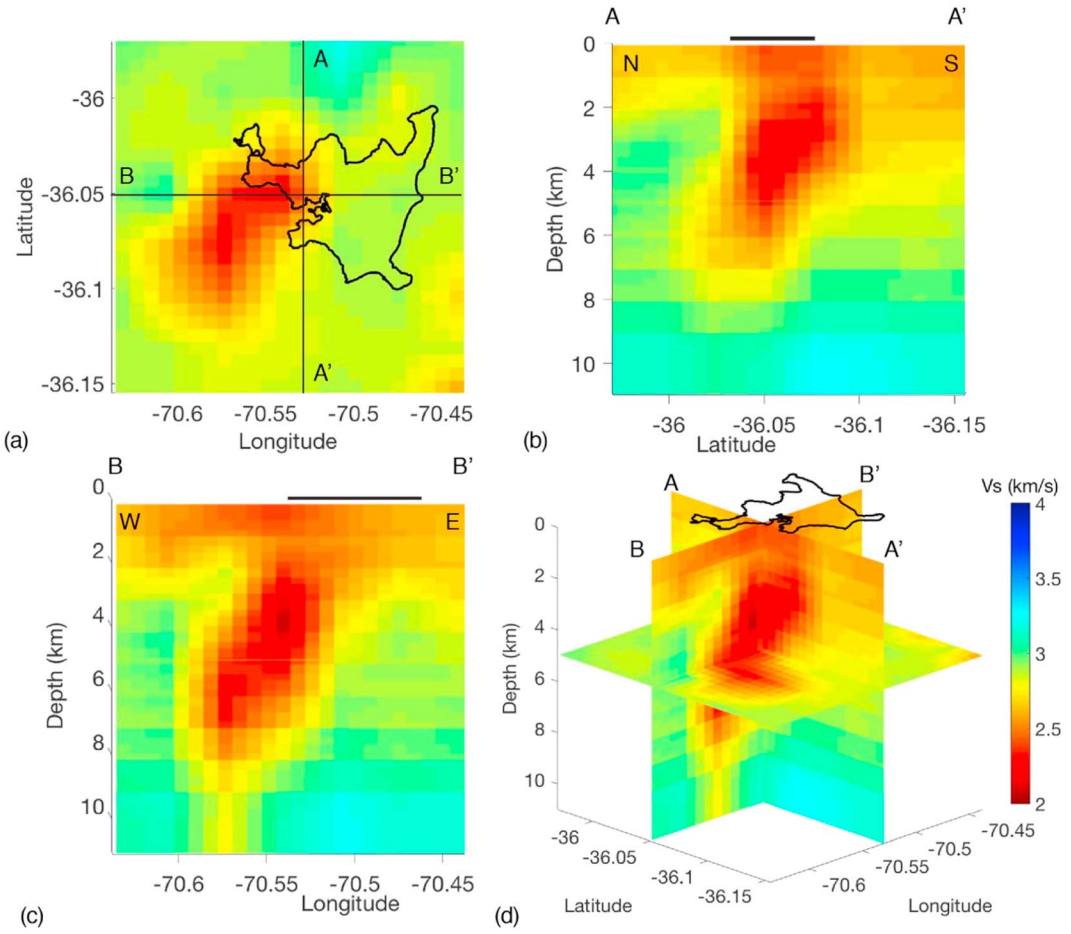

Figure 6. (a) Map of 4-km-depth slice, (b) north-south cross section, (c) west-east cross-section, and (d) perspective view (from the southwest) of the three-dimensional V_S structure beneath Laguna del Maule. Depths are relative to average surface elevation (~2,500 m).

We estimated percent melt using the approach of Flinders and Shen (2017), assuming that every reduction of 0.07 km/s in V_S from surrounding velocities corresponds to 1% melt. We obtained an average melt percentage of approximately 5%, corresponding to ~23 km^3 of melt. These results are similar in estimated reservoir volume, percent melt, and melt volume to the results for Mount St. Helens (Flinders & Shen, 2017) and are about two-thirds the melt volume estimated from the LdM gravity study (Miller, Williams-Jones, et al., 2017). A second estimate using an analytical relationship (Watanabe, 1993) yields the same average melt percent value. For the maximum −28% V_S anomaly, the melt percentage estimate is 11%. However, we recognize that the accuracy of such estimates is hindered by the tendency for tomographic inversions to smear out features and underestimate the amplitude of low-velocity anomalies due to imperfect resolution. The true volume of the low-V_S body is likely somewhat smaller and the true average melt percentage somewhat higher than our estimated average values. Furthermore, melt is likely concentrated in domains that are well below the resolution capability of our tomographic imaging, so that locally, melt percentage can be much higher than our average estimate. Based on calculated model resolution and uncertainty, the checkerboard tests, and surface-wave depth sensitivity kernels, features with dimensions smaller than ~6 km horizontally and ~3 km vertically or V_S perturbations less than ~0.1 km/s would not be adequately resolved with the available data.

4.2. Comparison With Existing Geophysical Observations

When integrating geophysical observations, it is critical to recognize the uncertainties and nonuniqueness of each model and the different physical parameters to which each is sensitive. In Figure 7 we compare the locations of the V_S, resistivity, and density anomalies on a cross section along the southwest edge of the

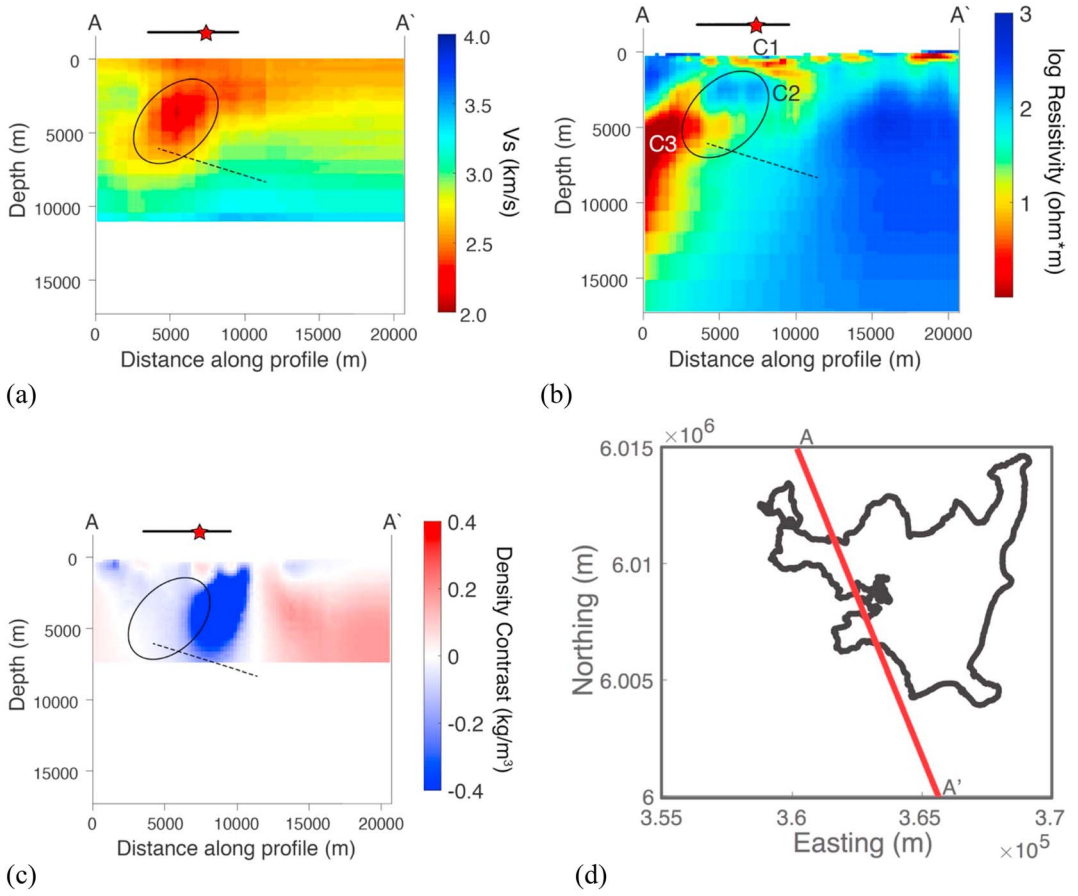

Figure 7. Comparison of (a) elliptical approximation to the low-V_S anomaly to the (b) resistivity and (c) density anomalies on (d) profile AA′ along the southwest edge of the lake. In (a)–(c), the black bar indicates where the profile crosses the lake, the red star indicates the center of inflation, and the intersection of the modeled sill (Feigl et al., 2014) with the cross sections is indicated by the dipping dashed line. Depths are relative to average surface elevation. No vertical exaggeration.

lake, through the center of uplift. The location of the low-V_S body and its NE-SW elongation agree reasonably well with the surface deformation pattern observed via InSAR (Figure 2) and supported by GNSS geodesy (Feigl et al., 2014; Le Mével et al., 2015, 2016). The estimated depth for the inflation source of about 5 km below surface (Feigl et al., 2014; Le Mével et al., 2015, 2016) corresponds to the middle of the depth range of the low-V_S body. The location and depth of the 115-km^3 low-density zone (supporting information Figure S1a; Miller, Williams-Jones, et al., 2017) overlap those of our low-V_S body, and both possess a similar NE-SW elongation. The centers of the low-V_S and density anomalies are offset by about 4 km, which is close to the 3-km horizontal node spacing of the tomography model. The center of deformation lies between the centers of the low-V_S and low-density anomalies (Figure 7c). Both the V_S and density models are nonunique, so the two anomalies might coincide in reality. We note, however, that shifting the tomography grid by 1.5 km (half the node spacing) in either direction does not alter the position of the low-V_S body. The differences between these models may also reflect subsurface conditions. Gravity is more sensitive to small, melt-rich domains but less so to the lowest melt fraction magma for which the density will approach that of the shallow country rock. Thus, we conclude the low-V_S and density anomalies reflect the same crystal-rich mush reservoir associated with the center of deformation. The apparent discrepancies in the location and volume of these features may reflect the distribution of melt within the reservoir.

In contrast, the most prominent features identified by the MT survey at LdM (Cordell et al., 2018) are not located near the center of deformation. The inversion of MT data yields a 3D resistivity model with two relatively thin low-resistivity zones beneath portions of the lake (C1 ~100 m thick starting ~100 m below surface

and C2 ~1 km thick at ~1.1 km below surface) underlain by a zone of moderate resistivity, and a deeper, much larger low-resistivity body north-northwest of the lake (C3; Figures 7a, S1b, and S1c). The shallow conductors (C1 and C2; Figure 7a) partially overlap the locations of the V_S and gravity anomalies but neither C1 nor C2 is interpreted as melt bearing by Cordell et al. (2018). Thus, a low-resistivity body associated with the magma reservoir inferred from the V_S and density models is not observed.

The largest feature of the resistivity model that is within the lake basin (C3, supporting information Figure S1c) extends northward from the lake and is centered at about 6-km depth (below surface). Although it is at a somewhat similar depth range (1 to 5 km below surface) to that of the low-density and low-V_S bodies, its center is situated ~10 km to the north, with some overlap at its southeastern, upper tip.

The fact that MT does not image a conductor in the same location as the seismic anomaly could potentially be explained by the fact that the estimated average melt fraction of the seismic anomaly is relatively low (~5%). A rhyodacitic crystal mush that contains 5% interstitial rhyolitic melt with 4–5 wt% H_2O stored at low pressure and 750–800 °C, conditions consistent with mineral thermobarometry and thermodynamic modeling by Andersen, Singer, et al. (2017) and Andersen et al. (2018), would have a resistivity of 30–80 Ω·m for a well-connected melt (Cordell et al., 2018; Glover et al., 2000; Guo et al., 2016). However, given that a 5% melt fraction is below the melt connectivity transition (Rosenberg & Handy, 2005), the resistivity of the mush could be closer to 100 Ω·m (Glover et al., 2000). The region of the MT resistivity model that aligns with the low-V_S anomaly between 2- and 5-km depths has a resistivity of 80–100 Ω·m, which is in good agreement with the above estimates for a magma that comprises 95% crystals and 5% interstitial rhyolitic melt (Figure 7b).

Neither the density nor V_S model show anomalies consistent with the C3 and C4 conductors to the north of the lake, although there is some overlap between C3 and the low-V_S body (supporting information Figure S1c). The northern perimeter of the LdM basin is underlain by the 990-ka Bobadilla Caldera, a major locus of magmatism and crustal fracturing that preceded the postglacial rhyolitic system. Moreover, unlike that in the southwest, the northwestern portion of the lake basin is penetrated by many northeast trending faults and mafic dikes, as well as late Pleistocene basaltic andesitic and andesitic vents (Hildreth et al., 2010) that may reflect conduits tapping the deeper portion of the larger transcrustal magma system imaged as C3 and C4 using MT (Figure 7). The C4 anomaly lies primarily outside the seismic and gravity model domains and is likely not able to be imaged with the current arrays. The lack of a low-density anomaly associated with C3 indicates this features has a density close to 2,400 kg/m^3, the reference density used by Miller, Williams-Jones, et al. (2017) to interpret the gravity data. Cordell et al. (2018) interpret C3 as intermediate to silicic magma with associated hydrothermal fluid. The absence of a low-V_S anomaly colocated with C3 may be due to reduced seismic resolution at depth to the north. Another possibility is that C3 primarily reflects highly conductive brine lenses (Afanasyev et al., 2018), which would significantly lower the bulk resistivity while having a relatively small impact on the bulk seismic velocity.

The 30-km^3, very low density (1,800–1,900 kg/m^3) feature interpreted by Miller, Williams-Jones, et al. (2017) as crystal-poor rhyolite and exsolved fluid may be too small to be resolved by the V_S model. In an attempt to reconcile the density anomaly with the MT results, sensitivity testing by Cordell et al. (2018) indicated that a melt-rich body below the center of deformation would need to be at least 30% smaller and/or lower melt fraction (e.g., <50% melt) than proposed by Miller, Williams-Jones, et al. (2017) to remain undetected by MT. Nevertheless, this feature of the density model suggests the presence of high-melt-fraction domains and thus a heterogeneous distribution of melt within the otherwise crystal-rich reservoir defined by the low-V_S anomaly.

Future seismic-gravity and seismic-MT joint inversions may help resolve the spatial offsets in these models and further elucidate possible gradients in the physical and compositional characteristics of the magma system. Jointly inverting all three data types directly is currently not feasible, but a sequential, structurally constrained inversion approach using the cross-product of the spatial gradients of the models (Gao & Zhang, 2018) might be successful.

4.3. Comparison With Petrologic Models

Geologic, petrologic, geochronologic, and geomorphic findings at LdM have contributed to a model of a voluminous, crystal-rich magma reservoir that has grown and persisted beneath the LdM lake basin for at least 60 kyr (Andersen et al., 2019; Andersen, Singer, et al., 2017; Hildreth et al., 2010; Singer et al., 2014).

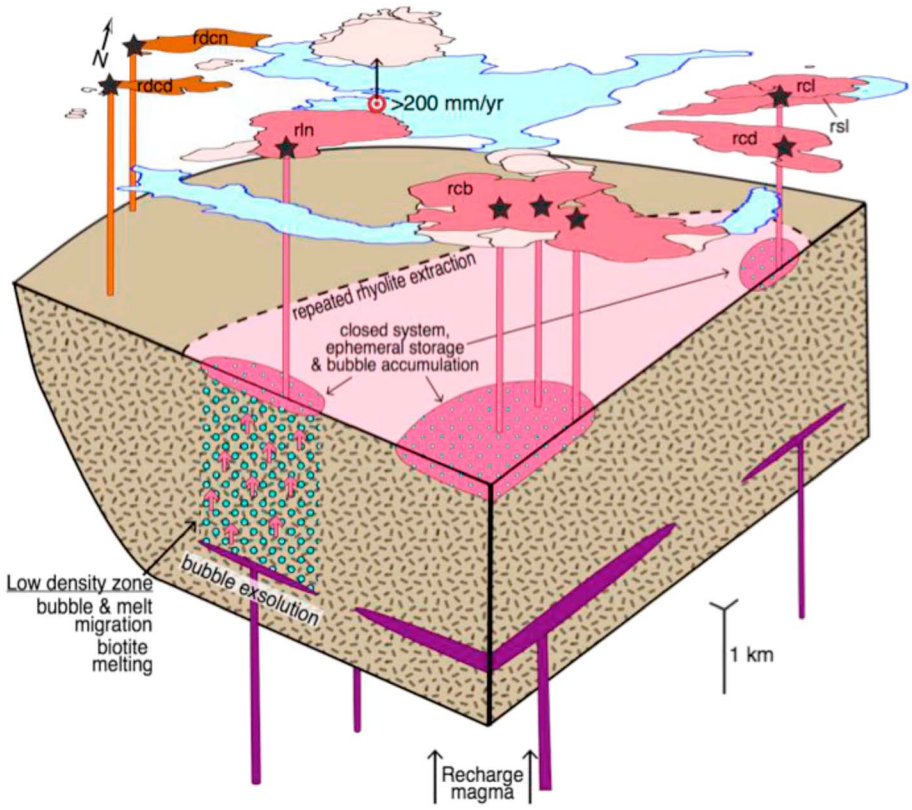

Figure 8. Cut-away schematic diagram of a model for the structure of the magmatic system beneath Laguna del Maule (LdM), viewed from the southeast, synthesizing the petrologic studies at LdM. A zone of low density and high melt fraction is embedded within a large crystal mush zone, consistent with that imaged by the surface-wave tomography. The configuration of the modern magma reservoir derived from the V_S, resistivity, and density models is consistent with that inferred from the petrologic studies. Consequently, the processes that catalyzed the recent rhyolite eruptions at LdM likely continue to this day. LdM and nearby lakes are in blue, the most recent lava flows and associated vents are in dark pink, and some older lava flows are in light pink. Vertical dark pink lines schematically indicate hypothetical magma conduits. Five times vertical exaggeration. From Andersen et al. (2018).

Much of this reservoir persisted in a near-solidus state. However, repeated intrusion of magma ascending from the deep crust during postglacial times has heated the reservoir from below. These additions of heat and volatiles to the crystal-rich reservoir thermally buffered bodies of higher-melt-fraction mush (30–50% melt) and contributed to the segregation of discrete, modest-volume, eruptible rhyolitic magma bodies (Andersen et al., 2018, 2019). The residence time of rhyolite erupted during the late Holocene, derived from diffusion chronometry of trace element zoning in feldspars, favors a timescale of extraction to eruption of rhyolitic melt on the order of decades to centuries and suggests its in situ volumes did not substantially exceed the erupted volumes, <3 km^3 (Figure 8; Andersen et al., 2018).

The geophysical data collected to date are consistent with a magma system that conforms to these petrologic interpretations. The ~450-km^3 low-V_S body reflects a near-solidus magma reservoir. The low-density, high-melt-fraction domain identified in the Bouguer gravity inversion likely reflects a body of less crystallized mush, a thin bubble-rich melt layer, and possibly eruptible magma (>50% melt; Marsh, 2015; Miller, Williams-Jones, et al., 2017; Parmigiani et al., 2016; Andersen et al., 2018). Thus, taken together, the seismic, gravity, and MT observations suggest that the processes that have catalyzed rhyolitic eruptions at LdM since the late Pleistocene remain active to this day.

5. Conclusions

Surface-wave tomography has identified a 450-km^3 low-V_S domain that is consistent with a crystal-rich magma reservoir residing beneath LdM. The interpretation of the V_S model—in light of the existing

gravity, MT, and geodetic observations—reveals a shallow reservoir with local heterogeneities in melt content that is fed by a deeper magma system to the north. Although some discrepancies among the geophysical models persist, together they yield a more nuanced perspective of the magma system than any individual method alone. Future joint inversions of the seismic, gravity, and MT data will aim to refine this picture. The low-V_S body is approximately coincident with the current center of decade-long inflation at >20 cm/year and is only a few kilometers north of the vent for the Nieblas rhyolite flow (Figure 1a) that is likely the most recent eruptive product and is the largest single lava flow (~1.2 km^3) in the basin (Hildreth et al., 2010). The similarity of the petrologic and geophysical models of the LdM magma system suggests a future eruption of similar style and magnitude to the recent rhyolites is likely. Explosive eruption of even a small fraction of the estimated melt distributed within the low-V_S body, for example 10%, ~2 km^3, would produce an eruption similar to the Nieblas event that would have a major impact on the surrounding region (Fierstein, 2018). Eruption of the entirety of the modeled melt volume, 23 km^3, would have a much more substantial damage potential. Continuous seismic and geodetic monitoring of LdM is a priority of Chile's national volcano observatory and is essential to forecasting this hazard.

Acknowledgments
This research was supported by the National Science Foundation Integrated Earth Systems program grant EAR-141179. We thank the many people who contributed to the seismic fieldwork, especially Neal Lord, Peter Sobol, Sergio Morales Méndez, Diego Lobos Lilo, Tim Clements, Francisco Delgado, Susanna Webb, Óscar Valderrama, and Costanza Perales. Luis Torres is thanked for logistics support and for ensuring safety during operations at Laguna del Maule. We thank two anonymous reviewers for their detailed comments. The seismic data supporting the analysis and conclusions presented here can be accessed via the IRIS Data Management Center, experiment ZR 2015-2018.

References

Afanasyev, A., Blundy, J., Melnik, O., & Sparks, S. (2018). Formation of magmatic brine lenses via focussed fluid-flow beneath volcanoes. *Earth and Planetary Science Letters*, *486*, 119–128.

Andersen, N. L., Jicha, B. R., Singer, B. S., & Hildreth, W. (2017). Incremental heating of Bishop Tuff sanidine reveals pre-eruptive radiogenic Ar and rapid remobilization from cold storage. *Proceedings of the National Academy of Sciences*, *114*(47), 12,407–12,412. https://doi.org/10.1073/pnas.1709581114

Andersen, N. L., Singer, B. S., & Coble, M. A. (2019). Repeated rhyolite eruptions from heterogeneous hot zones embedded within a cool, shallow magma reservoir. *Journal of Geophysical Research: Solid Earth*, *124*. https://doi.org/10.1029/2018JB016418

Andersen, N. L., Singer, B. S., Costa, F., Fournelle, J. F., Herrin, J., & Fabbro, G. (2018). Petrochronologic perspectives on rhyolite volcano unrest at Laguna del Maule, Chile. *Earth and Planetary Science Letters*, *493*, 57–70.

Andersen, N. L., Singer, B. S., Jicha, B. R., Beard, B. L., Johnson, C. M., & Licciardi, J. M. (2017). Pleistocene to Holocene growth of a large upper crustal rhyolitic magma reservoir beneath the active Laguna del Maule volcanic field, central Chile. *Journal of Petrology*, *58*(1), 85–114. https://doi.org/10.1093/petrology/egx006

Aster, R., Borchers, B., & Thurber, C. (2012). *Parameter estimation and inverse problems* (2nd ed., p. 360). Waltham, MA: Elsevier.

Bachmann, O., & Bergantz, G. W. (2004). On the origin of crystal-poor rhyolites: Extracted from batholithic crystal mushes. *Journal of Petrology*, *45*(8), 1565–1582. https://doi.org/10.1093/petrology/egh019

Barboni, M., Boehnke, P., Schmitt, A. K., Harrison, T. M., Shane, P., Bouvier, A. S., & Baumgartner, L. (2016). Warm storage for arc magmas. *Proceedings of the National Academy of Sciences*, *113*(49), 13,959–13,964. https://doi.org/10.1073/pnas.1616129113

Bensen, G. D., Ritzwoller, M. H., Barmin, M. P., Levshin, A. L., Lin, F., Moschetti, M. P., et al. (2007). Processing seismic ambient noise data to obtain reliable broad-band surface wave dispersion measurements. *Geophysical Journal International*, *169*(3), 1239–1260. https://doi.org/10.1111/j.1365-246X.2007.03374.x

Campillo, M., & Paul, A. (2003). Long-range correlations in the diffuse seismic coda. *Science*, *299*(5606), 547–549. https://doi.org/10.1126/science.1078551

Campillo, M., Roux, P., & Shapiro, N. M. (2011). Correlations of seismic ambient noise to image and to monitor the solid Earth. In H. K. Gupta (Ed.), *Encyclopedia solid Earth geophysics* (pp. 1230–1235). Dordrecht, Netherlands: Springer.

Cardona, C., Tassara, A., Gil-Cruz, F., Lara, L., Morales, S., Kohler, P., & Franco, L. (2018). Crustal seismicity associated to rapid surface uplift at Laguna del Maule volcanic complex, southern volcanic zone of the Andes. *Journal of Volcanology and Geothermal Research*, *353*, 83–94. https://doi.org/10.1016/j.jvolgeores.2018.01.009

Cashman, K. V., Sparks, R. S. J., & Blundy, J. D. (2017). Vertically extensive and unstable magmatic systems: A unified view of igneous processes. *Science*, *355*, eaag3055.

Castro, J. M., & Dingwell, D. B. (2009). Rapid ascent of rhyolitic magma at Chaitén volcano, Chile. *Nature*, *461*, 783–780. https://doi.org/10.1038/nature08458

Comeau, M. J., Unsworth, M. J., & Cordell, D. (2016). New constraints on the magma distribution and composition beneath Volcán Uturuncu and the southern Bolivian Altiplano from magnetotelluric data. *Geosphere*, *12*(5), 1391–1421. https://doi.org/10.1130/GES01277.1

Cooper, K. M., & Kent, A. J. R. (2014). Rapid remobilization of magmatic crystals kept in cold storage. *Nature*, *506*(7489), 480–483. https://doi.org/10.1038/nature12991

Cordell, D., Unsworth, M. J., & Diaz, D. (2018). Imaging the Laguna del Maule volcanic field, central Chile, using magnetotellurics: Evidence for crustal melt regions laterally-offset from surface vents and Holocene lava flows. *Earth and Planetary Science Letters*, *488*, 168–180.

Druitt, T. H., Costa, F., Dungan, M., & Scaillet, B. (2012). Decadal to monthly timescales of magma transfer and reservoir growth at a caldera volcano. *Nature*, *482*(7383), 77–80. https://doi.org/10.1038/nature10706

Feigl, K. L., LeMével, H., Ali, S. T., Córdova, L., Andersen, N. L., DeMets, C., & Singer, B. S. (2014). Rapid uplift in Laguna del Maule volcanic field of the Andean Southern Volcanic Zone (Chile) 2007–2012. *Geophysical Journal International*, *196*(2), 885–901. https://doi.org/10.1093/gji/ggt438

Feng, C.-C., & Teng, T. (1983). An error analysis of frequency-time analysis. *Bulletin of the Seismological Society of America*, *73*, 143–155.

Fierstein, J. (2018). Postglacial eruptive history established by mapping and tephra stratigraphy provides perspectives on magmatic system beneath Laguna del Maule, Chile. AGU Chapman Conference, Integrating Geophysical, Petrochronologic, and Modeling Perspectives on Large Silicic Magma Systems, Quinamavida, Chile January 7–12, 2018, Abstract 328093.

Flinders, A. F., & Shen, Y. (2017). Seismic evidence for a possible deep crustal hot zone beneath Southwest Washington. *Scientific Reports*, *7*(1), 7400. https://doi.org/10.1038/s41598-017-07123-w

Fournier, T. J., Pritchard, M. E., & Riddick, S. N. (2010). Duration, magnitude, and frequency of subaerial volcano deformation events: New results from Latin America using InSAR and a global synthesis. *Geochemistry, Geophysics, Geosystems*, *11*, Q01003. https://doi.org/10.1029/2009GC002558

Gao, J., & Zhang, H. (2018). An efficient sequential strategy for realizing cross-gradient joint inversion: Method and its application to two-dimensional cross borehole seismic travel time and DC resistivity tomography. *Geophysical Journal International*, *213*(2), 1044–1055. https://doi.org/10.1093/gji/ggy026

Glover, P. W. J., Pous, J., Queralt, P., Munoz, J. A., Liesa, M., & Hole, M. J. (2000). Integrated two dimensional lithospheric conductivity modelling in the Pyrenees using field scale and laboratory measurements. *Earth and Planetary Science Letters*, *178*, 59–72.

Guo, X., Chen, Q., & Ni, H. (2016). Electrical conductivity of hydrous silicate melts and aqueous fluids: Measurement and applications. *Science China Earth Sciences*, *59*(5), 889–900. https://doi.org/10.1007/s11430-016-5267-y

Hildreth, W. (2004). Volcanological perspectives on Long Valley, Mammoth Mountain, and Mono Craters: Several contiguous but discrete systems. *Journal of Volcanology and Geothermal Research*, *136*(3-4), 169–198. https://doi.org/10.1016/j.jvolgeores.2004.05.019

Hildreth, W., Godoy, E., Fierstein, J., & Singer, B. (2010). Laguna del Maule volcanic field: Eruptive history of a Quaternary basalt-to-rhyolite distributed volcanic field on the Andean range crest in central Chile, *Servicio Nacional de Geología y Minería-Chile,* Boletin, 63, 142 pp.

Hildreth, W., & Moorbath, S. (1988). Crustal contributions to arc magmatism in the Andes of central Chile. *Contributions to Mineralogy and Petrology*, *98*(4), 455–489. https://doi.org/10.1007/BF00372365

Hill, G. J., Caldwell, T. G., Heise, W., Chertkoff, D. G., Bibby, H. M., Burgess, M. K., et al. (2009). Distribution of melt beneath Mount St Helens and Mount Adams inferred from magnetotelluric data. *Nature Geoscience*, *2*(11), 785–789. https://doi.org/10.1038/ngeo661

Huang, H.-H., Lin, F.-C., Schmandt, B., Farrell, J., Smith, R. B., & Tsai, V. C. (2015). The Yellowstone magmatic system from the mantle plume to the upper crust. *Science*, *348*(6236), 773–776. https://doi.org/10.1126/science.aaa5648

Jackson, M. D., Blundy, J., & Sparks, R. S. J. (2018). Chemical differentiation, cold storage and remobilization of magma in the Earth's crust. *Nature*, *564*, 405–409. https://doi.org/10.1038/s41586-018-0746-2

Jaxybulatov, K., Shapiro, N. M., Koulakov, I., Mordret, A., Landès, M., & Sens-Schönfelder, C. (2014). A large magmatic sill complex beneath the Toba caldera. *Science*, *346*(6209), 617–619. https://doi.org/10.1126/science.1258582

Jay, J., Costa, F., Pritchard, M., Lara, L., Singer, B., & Herrin, J. (2014). Locating magma reservoirs using InSAR and petrology before and during the 2011–2012 Cordon Caulle silicic eruption. *Earth and Planetary Science Letters*, *395*, 254–266. https://doi.org/10.1016/j.epsl.2014.03.046

Kukarina, E., West, M., Keyson, L. H., Koulakov, I., Tsibizov, L., & Smirnov, S. (2017). Focused magmatism beneath Uturuncu volcano, Bolivia: Insights from seismic tomography and deformation modeling. *Geosphere*, *13*(6), 1855–1866. https://doi.org/10.1130/GES01403.1

Le Mével, H., Feigl, K. L., Córdova, L., DeMets, C., & Lundgren, P. (2015). Evolution of unrest at Laguna del Maule volcanic field (Chile) from InSAR and GPS measurements, 2003 to 2014. *Geophysical Research Letters*, *42*, 6590–6598. https://doi.org/10.1002/2015GL064665

Le Mével, H., Gregg, P. M., & Feigl, K. L. (2016). Magma injection into a long-lived reservoir to explain geodetically measured uplift: Application to the 2007–2014 unrest episode at Laguna del Maule volcanic field, Chile. *Journal of Geophysical Research: Solid Earth*, *121*, 6092–6108. https://doi.org/10.1002/2016JB013066

Lees, J. (2007). Seismic tomography of magmatic systems. *Journal of Volcanology and Geothermal Research*, *167*(1-4), 37–56. https://doi.org/10.1016/j.jvolgeores.2007.06.008

Lowenstern, J. B., Smith, R. B., & Hill, D. P. (2006). Monitoring super-volcanoes: Geophysical and geochemical signals at Yellowstone and other large caldera systems. *Philosophical Transactions of the Royal Society A: Mathematical, Physical and Engineering Sciences*, *364*(1845), 2055–2072. https://doi.org/10.1098/rsta.2006.1813

Magee, C., Stevenson, C. T. E., Ebmeier, S. K., Keir, D., Hammond, J. O. S., Gottsmann, J. H., et al. (2018). Magma plumbing systems: A geophysical perspective. *Journal of Petrology*, *59*(6), 1217–1251 https://doi.org/10.1093/petrology/egy064

Marsh, B. D. (2015). Magma chambers. In *The encyclopedia of volcanoes*, Sigurdsson, Houghton, McNutt, Rymer, Stix, (pp. 185–201). Academic Press.

Masterlark, T., Haney, M. M., Dickinson, H., Fournier, T., & Searcy, C. (2010). Rheologic and structural controls on the deformation of Okmok volcano, Alaska: FEMs, InSAR, and ambient noise tomography. *Journal of Geophysical Research*, *115*, B02409. https://doi.org/10.1029/2009JB006324

Miller, C. A., LeMével, H., Currenti, G., Williams-Jones, G., & Tikoff, B. (2017). Microgravity changes at the Laguna del Maule volcanic field: Magma-induced stress changes facilitate mass addition. *Journal of Geophysical Research: Solid Earth*, *122*, 3179–3196. https://doi.org/10.1002/2017JB014048

Miller, C. A., & Williams-Jones, G. (2016). Internal structure and volcanic hazard potential of Mt Tongariro, New Zealand, from 3D gravity and magnetic models. *Journal of Volcanology and Geothermal Research*, *319*, 12–28. https://doi.org/10.1016/j.jvolgeores.2016.03.012

Miller, C. A., Williams-Jones, G., Fournier, D., & Witter, J. (2017). 3-D gravity inversion and thermodynamic modelling reveal properties of shallow silicic magma reservoir beneath Laguna del Maule, Chile. *Earth and Planetary Science Letters*, *459*, 14–27.

Parks, M. M., Biggs, J., England, P., Mather, T. A., Nomikou, P., Palamartchouk, K., et al. (2012). Evolution of Santorini Volcano dominated by episodic and rapid fluxes of melt from depth. *Nature Geoscience*, *5*(10), 749–754. https://doi.org/10.1038/ngeo1562

Parmigiani, A., Faroughi, S., Huber, C., Bachmann, O., & Su, Y. (2016). Bubble accumulation and its role in the evolution of magma reservoirs in the upper crust. *Nature*, *532*(7600), 492–495. https://doi.org/10.1038/nature17401

Pritchard, M. E., & Gregg, P. M. (2016). Geophysical evidence for silicic crustal melt in the continents: Where, what kind, and how much? *Elements*, *12*(2), 121–127. https://doi.org/10.2113/gselements.12.2.121

Rosenberg, C. L., & Handy, M. R. (2005). Experimental deformation of partially melted granite revisited: implications for the continental crust *Journal of Metamorphic Geology*, *23*(1), 19–28.

Rubin, A. E., Cooper, K. M., Till, C. B., Kent, C. A. J. R., Costa, F., Bose, M., et al. (2017). Rapid cooling and cold storage in a silicic magma reservoir recorded in individual crystals. *Science*, *356*(6343), 1154–1156. https://doi.org/10.1126/science.aam8720

Self, S., & Blake, S. (2008). Consequences of explosive supereruptions. *Elements*, *4*(1), 41–46. https://doi.org/10.2113/GSELEMENTS.4.1.41

Singer, B. S., Andersen, N. L., LeMével, H., Feigl, K. L., DeMets, C., Tikoff, B., et al. (2014). Dynamics of a large, restless, rhyolitic magma system at Laguna del Maule, southern Andes Chile. *GSA Today*, *24*, 4–10.

Singer, B. S., Costa, F., Herrin, J. S., Hildreth, W., & Fierstein, J. (2016). The timing of compositionally-zoned magma reservoirs and mafic 'priming' weeks before the 1912 Novarupta-Katmai rhyolite eruption. *Earth and Planetary Science Letters*, *451*, 125–137.

Singer, B. S., Le Mével, H., Licciardi, J. M., Córdova, L., Tikoff, B., Garibaldi, N., et al. (2018). Geomorphic expression of rapid Holocene silicic magma reservoir growth beneath Laguna del Maule, Chile. *Science Advances*, *4*(6), eaat1513. https://doi.org/10.1126/sciadv.aat1513

Sparks, R. S. J., Self, S., Pyle, D., Oppenheimer, C., Rymer, H., & Grattan, J. (2005). *Supereruptions: Global effects and future threats*. Report of a Geological Society of London Working Group.

Szymanowski, D., Wotzlaw, J.-F., Ellis, B. S., Bachmann, O., Guillong, M., & von Quadt, A. (2017). Protracted near-solidus storage and pre-eruptive rejuvenation of large magma reservoirs. *Nature Geoscience*, *10*(10), 777–782. https://doi.org/10.1038/ngeo3020

Thurber, C., & Eberhart-Phillps, D. (1999). Local earthquake tomography with flexible gridding. *Computers & Geosciences*, *25*(7), 809–818. https://doi.org/10.1016/S0098-3004(99)00007-2

Um, J., & Thurber, C. (1987). A fast algorithm for two-point seismic ray tracing. *Bulletin of the Seismological Society of America*, *77*, 972–986.

Ward, K. M., Zandt, G., Beck, S. L., Christensen, D. H., & McFarlin, H. (2014). Seismic imaging of the magmatic underpinnings beneath the Altiplano-Puna volcanic complex from the joint inversion of surface wave dispersion and receiver functions. *Earth and Planetary Science Letters*, *404*, 43–53. https://doi.org/10.1016/j.epsl.2014.07.022

Watanabe, T. (1993). Effects of water and melt on seismic velocities and their application to characterization of seismic reflectors. *Geophysical Research Letters*, *20*(24), 2933–2936. https://doi.org/10.1029/93GL03170

Yang, Y. (2014). Application of teleseismic long-period surface waves from ambient noise in regional surface wave tomography: A case study in western USA. *Geophysical Journal International*, *198*(3), 1644–1652. https://doi.org/10.1093/gji/ggu234

Yao, Y., van der Hilst, R., & de Hoop, M. (2006). Surface-wave array tomography in SE Tibet from ambient seismic noise and two-station analysis—I. Phase velocity maps. *Geophysical Journal International*, *166*(2), 732–744. https://doi.org/10.1111/j.1365-246X.2006.03028.x